The Astrophysical Journal, 890:62 (8pp), 2020 February 10 https://doi.org/10.3847/1538-4357/ab6987

Deep *XMM-Newton* Observations Reveal the Origin of Recombining Plasma in the Supernova Remnant W44

Hiromichi Okon[1], Takaaki Tanaka[1], Hiroyuki Uchida[1], Hiroya Yamaguchi[2], Takeshi Go Tsuru[1], Masumichi Seta[3], Randall K. Smith[4], Satoshi Yoshiike[5], Salvatore Orlando[6], Fabrizio Bocchino[6], and Marco Miceli[6,7]
[1] Department of Physics, Kyoto University, Kitashirakawa Oiwake-cho, Sakyo, Kyoto 606-8502, Japan; okon@cr.scphys.kyoto-u.ac.jp
[2] Institute of Space and Astronautical Science, JAXA, 3-1-1 Yoshinodai, Chuo, Sagamihara, Kanagawa 252-5210, Japan
[3] Department of Physics, School of Science and Technology, Kwansei Gakuin University, 2-1 Gakuen, Sanda, Hyogo 669-1337, Japan
[4] Harvard-Smithsonian Center for Astrophysics, 60 Garden St, Cambridge, MA 02138, USA
[5] Department of Physics, Nagoya University, Furo-cho, Chikusa, Nagoya, Aichi 464-8601, Japan
[6] INAF-Osservatorio Astronomico di Palermo, Piazza del Parlamento 1, I-90134 Palermo, Italy
[7] Dipartimento di Fisica e Chimica E. Segre, Universita degli studi di Palermo, Piazza del Parlamento 1, I-90134 Palermo, Italy
Received 2019 September 13; revised 2019 November 20; accepted 2019 December 16; published 2020 February 12

Abstract

Recent X-ray studies have revealed overionized recombining plasmas in a dozen mixed-morphology (MM) supernova remnants (SNRs). However, the physical process of the overionization has not yet been fully understood. Here we report on spatially resolved spectroscopy of X-ray emission from W44, one of the overionized MM SNRs, using *XMM-Newton* data from deep observations, with the aim of clarifying the physical origin of the overionization. We find that combination of low electron temperature and low recombination timescale is achieved in the region interacting with dense molecular clouds. Moreover, a clear anticorrelation between the electron temperature and the recombination timescale is obtained from each of the regions with and without the molecular clouds. The results are well explained if the plasma was overionized by rapid cooling through thermal conduction with the dense clouds hit by the blast wave of W44. Given that a few other overionized SNRs show evidence for adiabatic expansion as the major driver of the rapid cooling, our new result indicates that both processes can contribute to overionization in SNRs, with the dominant channel depending on the evolutionary stage.

Unified Astronomy Thesaurus concepts: Supernova remnants (1667); Molecular clouds (1072); X-ray astronomy (1810); Plasma astrophysics (1261)

1. Introduction

In the previously accepted scenario, plasmas in supernova remnants (SNRs) were believed to be collisionally ionizing until they reached equilibrium. Thus, the ionization degree was expected to be equal to or below that in collisional ionization equilibrium (CIE). The standard scenario, however, was questioned by Kawasaki et al. (2002). Analyzing *ASCA* data of IC 443, they measured the ionization degree of S ions based on a Lyα-to-Heα line intensity ratio, implying an ionization degree higher than that in CIE. *Suzaku* data then provided clearer evidence of overionization. Ozawa et al. (2009) and Yamaguchi et al. (2009) discovered strong radiative recombining continua (RRCs) in *Suzaku* data of W49B and IC 443, respectively, directly indicating that the plasmas are in a recombination-dominant state.

Overionized recombining plasmas (RPs) have since been discovered in a dozen SNRs (Uchida et al. 2015). All of these SNRs are classified as mixed-morphology (MM) SNRs, which are characterized by radio shells with center-filled X-ray emissions (Rho & Petre 1998). Most of the MM SNRs are known to be interacting with molecular clouds. These facts imply that the presence of the "recombination-dominant phase" is somewhat common among MM SNRs, and that shock–cloud interactions seem to be related to the origin of RPs. Based on spatially resolved spectroscopy of *Suzaku* data, some authors such as Matsumura et al. (2017a) and Okon et al. (2018) claimed that X-ray-emitting plasmas in, e.g., IC 443 and W28 were rapidly cooled due to thermal conduction with interacting molecular clouds, which resulted in the formation of the RPs as originally proposed by Kawasaki et al. (2002, 2005). Itoh & Masai (1989) and Shimizu et al. (2012) predicted another scenario, the so-called rarefaction scenario, in which rapid adiabatic expansion is responsible for the overionization. Some authors, e.g., Miceli et al. (2010), Lopez et al. (2013), Greco et al. (2018), and Sezer et al. (2019), indeed claimed that their X-ray spectroscopy results support this scenario. The clearest evidence was presented by Yamaguchi et al. (2018), who analyzed *NuSTAR* data of W49B and performed spatially resolved spectroscopy, focusing on the Fe RRC. With these observational results contradicting each other, the physical origin of RPs is not yet understood and is still under debate.

W44 (a.k.a. G34.7−0.4 or 3C 392) is a Galactic MM SNR with an estimated distance of ∼3 kpc (Claussen et al. 1997; Ranasinghe & Leahy 2018). The age of W44 is estimated to be ∼20 kyr (Smith et al. 1985; Wolszczan et al. 1991; Harrus et al. 1997). Wolszczan et al. (1991) discovered a radio pulsar, PSR B1853+01, in the southern part of the remnant, indicating that W44 is a remnant of a core-collapse supernova. W44 is known to be interacting with molecular clouds as evidenced by radio observations of OH masers at 1720 MHz (Frail & Mitchell 1998; Claussen et al. 1999) and ^{12}CO lines (Seta et al. 1998, 2004; Yoshiike et al. 2013). In the X-ray band, Jones et al. (1993) observed W44 with *Einstein* and reported that the emission is predominantly thermal, based on the presence of Mg, Si, and S emission lines. In *Suzaku* data, Uchida et al. (2012) found RRCs of Si and S, and concluded that the plasmas in the central bright region (Figure 1) are in an overionized state.

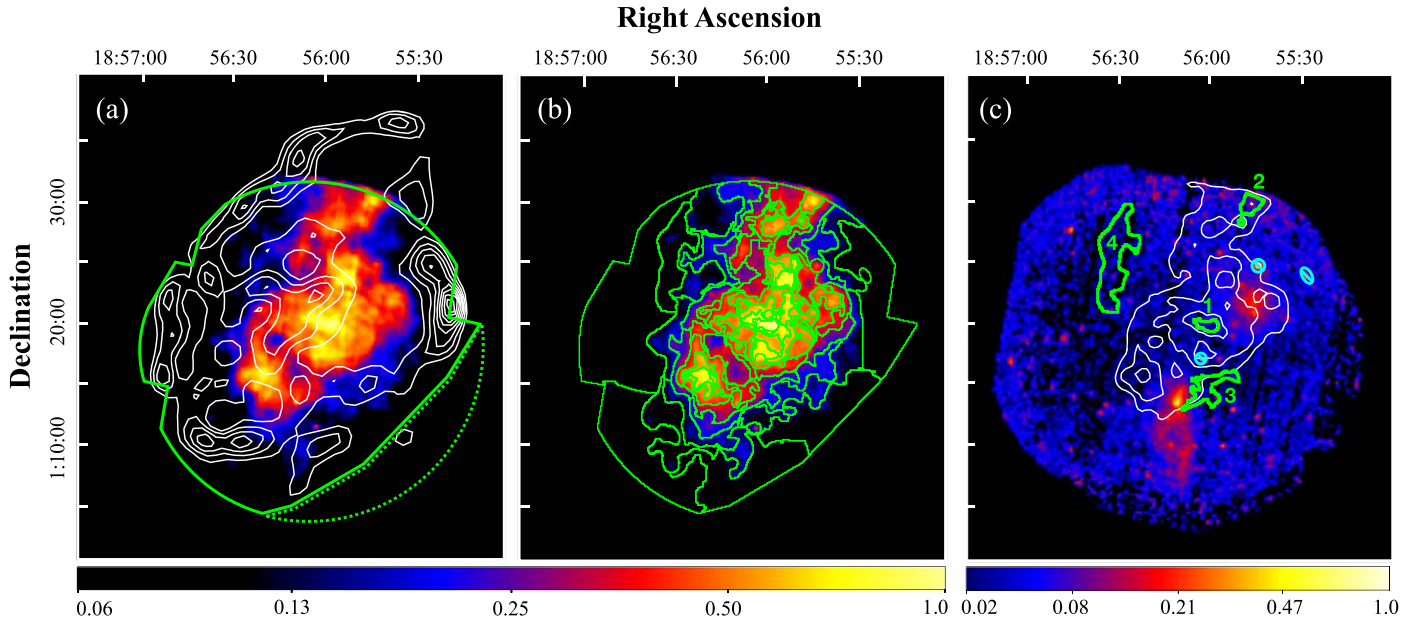

Figure 1. MOS+pn images of W44 in the energy band of (a), (b) 0.5–4.0 keV, and (c) 4.0–8.0 keV after non-X-ray background subtraction and correction for the vignetting effect. The coordinate refers to the J2000.0 epoch. The white contours in (a) indicate a radio continuum image at 1.4 GHz taken with the Karl G. Jansky Very Large Array whereas those in (c) are the 0.5–4.0 keV X-ray image. The source and background spectra were extracted from the regions enclosed by the solid and dashed lines in (a). The source region was divided into 70 subregions as shown in (b). The regions enclosed by the green lines in (c) are the four representative subregions whose spectra are plotted in Figure 2. The cyan ellipses are regions excluded in the spectral analysis to remove bright point sources.

Table 1
Observation Log

Target	Observation ID	Observation Date	(R.A., Decl.)[a]	Effective Exposure
W44 PWN	0551060101	2009 Apr 24	($18^h56^m11^s.00$, $+01°13'28''.0$)	65 ks
W44	0721630101	2013 Oct 18	($18^h56^m06^s.99$, $+01°17'54''.0$)	110 ks
W44	0721630201	2013 Oct 19	($18^h56^m06^s.99$, $+01°17'54''.0$)	92 ks
W44	0721630301	2013 Oct 23	($18^h56^m06^s.99$, $+01°17'54''.0$)	93 ks

Note.
[a] Equinox in J2000.0.

Here we report on results from a spatially resolved analysis of *XMM-Newton* data of deep observations of W44 to pin down the physical origin of the RP. Throughout the paper, errors are quoted at 90% confidence levels in the tables and text. Error bars shown in figures correspond 1σ confidence levels.

2. Observations

W44 was observed several times from 2003 to 2013 with *XMM-Newton*. We discarded data sets whose effective exposures are extremely short because of flaring backgrounds, As a result, four data sets (Obs. ID = 0551060101, 0721630101, 0721630201, and 0721630301) were left for further analysis. The details of the observations used are summarized in Table 1. In what follows, we analyze data obtained with the European Photon Imaging Camera (EPIC), which is composed of two MOS cameras (Turner et al. 2001) and one pn (Strüder et al. 2001) CCD camera.

Following the cookbook for analysis procedures of extended sources,[8] we reduced the data with the Science Analysis System software version 16.0.0 and the calibration database version 3.9 released in 2017 January 2.[9] We estimated the non-X-ray background (NXB) with `mos-back`. We generated the redistribution matrix files and the ancillary response files using `mos-spectra`. We used version 12.9.0u of the XSPEC software (Arnaud 1996) for the following spectral analysis. In the image analysis, we merged MOS1, MOS2, and pn data of the each observation for better photon statistics. In the spectral analysis, we only used the MOS data because of their lower detector background level than the pn data.

3. Analysis and Results

3.1. Imaging Analysis

Figure 1 shows vignetting- and exposure-corrected images of W44 taken with the EPIC after NXB subtraction. The soft-band image in Figure 1(a) reveals the center-filled morphology and small bright knots as already reported by Shelton et al. (2004) based on *Chandra* data. In order to perform a spatially resolved spectroscopic analysis, we applied the contour-binning algorithm (Sanders 2006) to the 0.5–4.0 keV image, and divided the source region in Figure 1(a) into 70 subregions as displayed in

[8] ftp://xmm.esac.esa.int/pub/xmm-esas/xmm-esas.pdf

[9] http://xmm2.esac.esa.int/docs/documents/CAL-TN-0018.pdf

Figure 1(b). The algorithm generates subregions along the structure of the surface brightness so that each subregion has almost the same signal-to-noise ratio. We manually excluded bright point sources identified in the hard band image in Figure 1(c).

3.2. Background Estimation

To estimate the X-ray background, we extracted spectra from the off-source region (Figure 1) in the fields of view of each observation. After subtracting the NXB from each of the spectra, we co-added them to perform spectral fitting. The applied model consists of the cosmic X-ray background (CXB), the Galactic ridge X-ray emission (GRXE), and Al and Si Kα lines of instrumental origin which are not included in the NXB spectra estimated with `mos-back` (Lumb et al. 2002). By referring to Kushino et al. (2002), the CXB component was expressed as a power law with a photon index of 1.4 and a 2–10 keV intensity of 6.38×10^{8} erg cm^{-2} s^{-1} sr^{-1}. We employed the GRXE model of Uchiyama et al. (2013), which is composed of the foreground emission (FE), the high-temperature plasma emission (HP), the low-temperature plasma emission (LP), and the emission from cold matter (CM). We used the Tübingen–Boulder interstellar medium (ISM) absorption model (TBabs; Wilms et al. 2000) to estimate the column density ($N_{\rm H}^{\rm GRXE}$) for the total Galactic absorption in the line of sight toward W44. Most of the parameters of GRXE were fixed to those shown by Uchiyama et al. (2013). Free parameters were $N_{\rm H}^{\rm GRXE}$, kT_e of the LP, and the normalization of each component. The normalization of Al I and Si I Kα lines were allowed to vary. The best-fit parameters are summarized in Table 2. We used the best-fit model to account for the X-ray background in the source spectra in Section 3.3.

3.3. Spectral Analysis

Figure 2 shows background-subtracted MOS spectra extracted from the representative four subregions shown in Figure 1(c), where emission lines from highly ionized Ne, Mg, Si, S, Ar, and Ca are clearly resolved. The Lyα-to-Heα ratios and the continuum shape below $\sim$2 keV are different from each other, suggesting significant region-to-region variations of plasma parameters and of absorption column densities. We first fitted spectra from all 70 subregions with a CIE model. All the fittings left hump-like residuals at $\sim$2.7 keV corresponding to the edge of the Si XIII RRC. The result implies that the X-ray-emitting plasma in W44 is overionized not only in a part of the remnant, as reported by Uchida et al. (2012) based on *Suzaku* data of the central region, but in the whole remnant.

We then fitted all spectra with the RP model VVRNEI (Foster et al. 2017) in XSPEC. The model describes emission from a thermal plasma n_et after an abrupt decrease of the electron temperature from $kT_{\rm init}$ to kT_e under an assumption that the plasma initially was in CIE. Using the TBabs model, we took into account photoelectric absorption by the foreground gas with the solar abundances of Wilms et al. (2000). We allowed the column density $N_{\rm H}$, the electron temperature kT_e, recombining timescale n_et, and normalization of the VVRNEI component to vary. The parameter $kT_{\rm init}$ was fixed in the fittings. We tried $kT_{\rm init}$ of 1.0, 2.0, 3.0, and 5.0 keV, and found that the data are best reproduced with $kT_{\rm init} = 1.0$ keV. We thus show results obtained with $kT_{\rm init}$ fixed at 1.0 keV in what follows. We note that parameters such as $N_{\rm H}$, kT_e, and n_et are

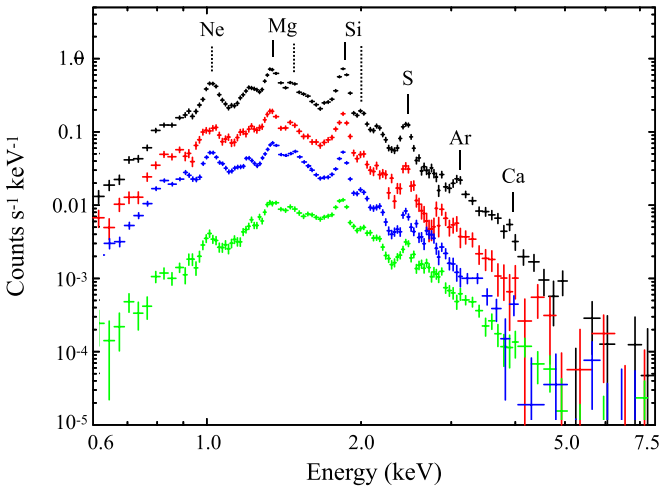

Figure 2. MOS (MOS1 + MOS2) spectra extracted from the subregions 1 (black), 2 (red), 3 (blue), and 4 (green), whose locations are shown in Figure 1(c). The NXB and X-ray background are subtracted. For display purposes, the spectra of Regions 3 and 4 are scaled by factors of 0.05 and 0.1, respectively. The vertical solid and dashed lines denote the centroid energies of the Heα lines and Lyα lines, respectively.

Table 2
Best-fit Model Parameters of the Background Spectrum

Component	Model Function	Parameter	Value
FE	TBabs (Absorption)	$N_{\rm H}^{\rm FE}$ (10^{22} cm^{-2})	0.56 (fixed)
	APEC (FE$_{\rm low}$)	kT_e (keV)	0.09 (fixed)
		$Z_{\rm all}$ (solar)	0.05 (fixed)
		Norm[a]	$1.05^{+0.12}_{-0.16}$
	APEC (FE$_{\rm high}$)	kT_e (keV)	0.59 (fixed)
		$Z_{\rm all}$	0.05 (fixed)
		Norm[a]	$\leqslant 1.68 \times 10^{-3}$
GRXE	TBabs (Absorption)	$N_{\rm H}^{\rm GRXE}$ (10^{22} cm^{-2})	$1.71^{+0.10}_{-0.03}$
	APEC (LP)	kT_e (keV)	$0.56^{+0.03}_{-0.03}$
		$Z_{\rm Ar}$	1.07 (fixed)
		$Z_{\rm other}$	0.81 (fixed)
		Norm[a]	$1.53^{+0.02}_{-0.01} \times 10^{-2}$
	APEC (HP)	kT_e (keV)	6.64 (fixed)
		$Z_{\rm Ar}$	1.07 (fixed)
		$Z_{\rm other}$	0.81 (fixed)
		Norm[a]	=LP Norm. $\times$ 0.29
	Power law (CM)	Γ	2.13 (fixed)
		Norm[b]	$\leqslant$0.20
	Gauss (CM; Fe I Kα)	Equivalent width (eV)	457 (fixed)
CXB	TBabs (Absorption)	$N_{\rm H}^{\rm CXB}$	$=N_{\rm H}^{\rm GRXE} \times 2$
	Power law	Γ	1.40 (fixed)
		Norm[b]	9.69 (fixed)
		χ^2_ν (ν)[c]	1.64 (229)

Notes.
[a] The unit is photons s^{-1} cm^{-2} keV^{-1} sr^{-1} at 1 keV.
[b] The emission measure integrated over the line of sight, i.e., $(1/4\pi D^2) \int n_e n_{\rm H} dl$ in units of 10^{-14} cm^{-5} sr^{-1}.
[c] The parameters χ^2_ν and ν indicate a reduced chi-squared and a degree of freedom, respectively.

Table 3
Best-fit Model Parameters of the Spectra from the Representative Subregions

Model Function	Parameters	Region 1	Region 2	Region 3	Region 4
TBabs	$N_{\rm H}$ (10^{22} cm^{-2})	$1.51^{+0.01}_{-0.03}$	1.43 ± 0.07	1.83 ± 0.03	2.8 ± 0.1
VVRNEI	kT_e (keV)	$0.503^{+0.019}_{-0.003}$	$0.55^{+0.04}_{0.03}$	$0.239^{+0.004}_{-0.002}$	0.26 ± 0.01
	$kT_{\rm init}$ (keV)	1.0 (fixed)	1.0 (fixed)	1.0 (fixed)	1.0 (fixed)
	$Z_{\rm Ne}$ (Solar)	$1.29^{+0.06}_{-0.07}$	0.8 ± 0.1	1.7 ± 0.1	3.0 ± 1.0
	$Z_{\rm Mg}$ (Solar)	$1.55^{+0.07}_{-0.05}$	1.1 ± 0.1	1.5 ± 0.1	$2.2^{+0.8}_{-0.4}$
	$Z_{\rm Si}$ (Solar)	$2.68^{+0.09}_{-0.05}$	1.7 ± 0.1	$2.6^{+0.2}_{-0.1}$	$2.6^{+0.9}_{-0.5}$
	$Z_{\rm S} = Z_{\rm Ar} = Z_{\rm Ca}$ (Solar)	2.1 ± 0.1	1.3 ± 0.2	$3.1^{+0.4}_{-0.2}$	3.2 ± 1.0
	$Z_{\rm Fe} = Z_{\rm Ni}$ (Solar)	$0.14^{+0.02}_{-0.01}$	$0.17^{+0.05}_{-0.04}$	1.1 ± 0.1	$1.0^{+0.6}_{-0.5}$
	$n_e t$ (10^{11} cm^{-3}s)	$5.3^{+0.2}_{-0.1}$	6.0 ± 0.1	6.0 ± 0.2	4.0 ± 0.3
	Norm[a]	$0.048^{+0.005}_{-0.003}$	$0.026^{+0.006}_{-0.005}$	0.11 ± 0.04	$0.19^{+0.02}_{-0.01}$
χ^2_ν (ν)[b]		1.45 (217)	1.12 (104)	1.57 (215)	1.25 (104)

Notes.
[a] The emission measure integrated over the line of sight, i.e., $(1/4\pi D^2)\int n_e n_{\rm H} dl$ in units of 10^{-14} cm^{-5} sr^{-1}.
[b] The parameters χ^2_ν and ν indicate a reduced chi-squared and a degree of freedom, respectively.

insensitive to the choice of $kT_{\rm init}$. The abundances of Ne, Mg, Si, S, and Fe were left free, whereas Ar and Ca were linked to S, and Ni was linked to Fe. The other abundances were fixed to the solar values. To the model for the W44 emission, we added the background model with the parameters fixed to those in Table 2. We allowed the normalizations of the Al and Si Kα lines to vary since the line intensities are known to have location-to-location variations on the detector plane (Kuntz & Snowden 2008).

In the fittings, we noticed line-like residuals at $\sim$1.2 keV in most of the subregions. Previous studies pointed out that the residuals are most probably due to the lack of Fe-L lines (e.g., Fe XVII $n > 6 \rightarrow n = 2$) in the atomic code (e.g., Matsumura et al. 2017a). However, the used NEI plasma code takes into account of the Fe-L lines (Foster et al. 2017). The residuals could be attributed to uncertainty in emissivity data of Fe-L lines in the code or to physical processes such as charge exchange that are not taken into account here. While the reason for the residuals is not clear, an addition of a Gaussian at 1.23 keV significantly improved the fits. In the case of Region 1 shown in Figure 3(a), the fitting statistic was improved from $\chi^2_\nu = 1.54$ with $\nu = 218$ to $\chi^2_\nu = 1.45$ with $\nu = 217$. On the other hand, the addition of the Gaussian did not change the parameters obtained beyond the 90% confidence level. In the spectral analyses, therefore, we used the model including the Gaussian.

Additional components are necessary to fit the spectra from the subregions where two extended hard sources are detected (Figure 1(c)). Nobukawa et al. (2018) pointed out that the northeastern source, which was discovered by Uchida et al. (2012), is probably a galaxy cluster. To account for the emission, therefore, we employed a CIE model, in which the abundance and kT_e were fixed to the values as determined by Matsumura (2018) while the normalization was left free. The southern source encompasses PSR B1853+01 and its associated pulsar wind nebula detected with *Chandra* (Petre et al. 2002). Since their X-ray emissions have featureless continuum spectra (Petre et al. 2002), we used a power-law model for the southern source, in which the photon index Γ and the normalization were free parameters.

All 70 spectra are well reproduced by the above RP (with an additional component) model. In addition to the result from Region 1 in Figure 3(a), we plot the best-fit models overlaid on the observed spectra from Regions 2–4 in Figures 3(b)–(d). The best-fit parameters in Regions 1–4 are summarized in Table 3. In a map in Figure 4, we present χ^2_ν values of each subregion, which range from 0.98 to 2.15. Among all 70 subregions, 20 subregions have $\chi^2_\nu \geqslant 1.5$, and four subregions have $\chi^2_\nu \geqslant 2.0$.

4. Discussion

4.1. Foreground Gas Distribution

The X-ray absorption column densities ($N_{\rm H}$) obtained from the spectral fittings present a tool to probe the spatial distribution of the gas in front of W44. Figure 5 shows a map of $N_{\rm H}$, where a significant spatial variation is clearly visible. The values, ranging from 1.3×10^{22} to 2.8×10^{22} cm^{-2}, are roughly consistent with the previous studies with *Suzaku* by Uchida et al. (2012) and Matsumura (2018), but the present map revealed a spatial distribution in much finer angular scales. We found that the X-ray absorption column densities are higher in the outer regions and are peaked in the northwestern rim. Based on CO line data, Seta et al. (2004) estimated column densities of foreground gas of $\sim 1 \times 10^{22}$ cm^{-2} and $\sim 2 \times 10^{22}$ cm^{-2} in the inner and outer regions, respectively, which agree well with our X-ray results. Note that the ISM around W44 is dominated by molecular gas and that the contribution from atomic gas amounts to only $\sim$10% of the total mass (Yoshiike et al. 2013). In the northwestern region with the highest X-ray absorption column density, it is known that a giant molecular cloud in the near side of W44 was hit by the SNR shock (Seta et al. 2004). When we select a velocity range of 40–50 km s^{-1}, which includes the most of the gas in the giant molecular cloud, the CO contours show almost a perfect match with the X-ray column density map (Figure 5(b)). According to Seta et al. (2004), the foreground gas in the northeastern rim has a column density of $N_{\rm H} \sim 3 \times 10^{22}$ cm^{-2}, which is again consistent with the values estimated from our X-ray analysis.

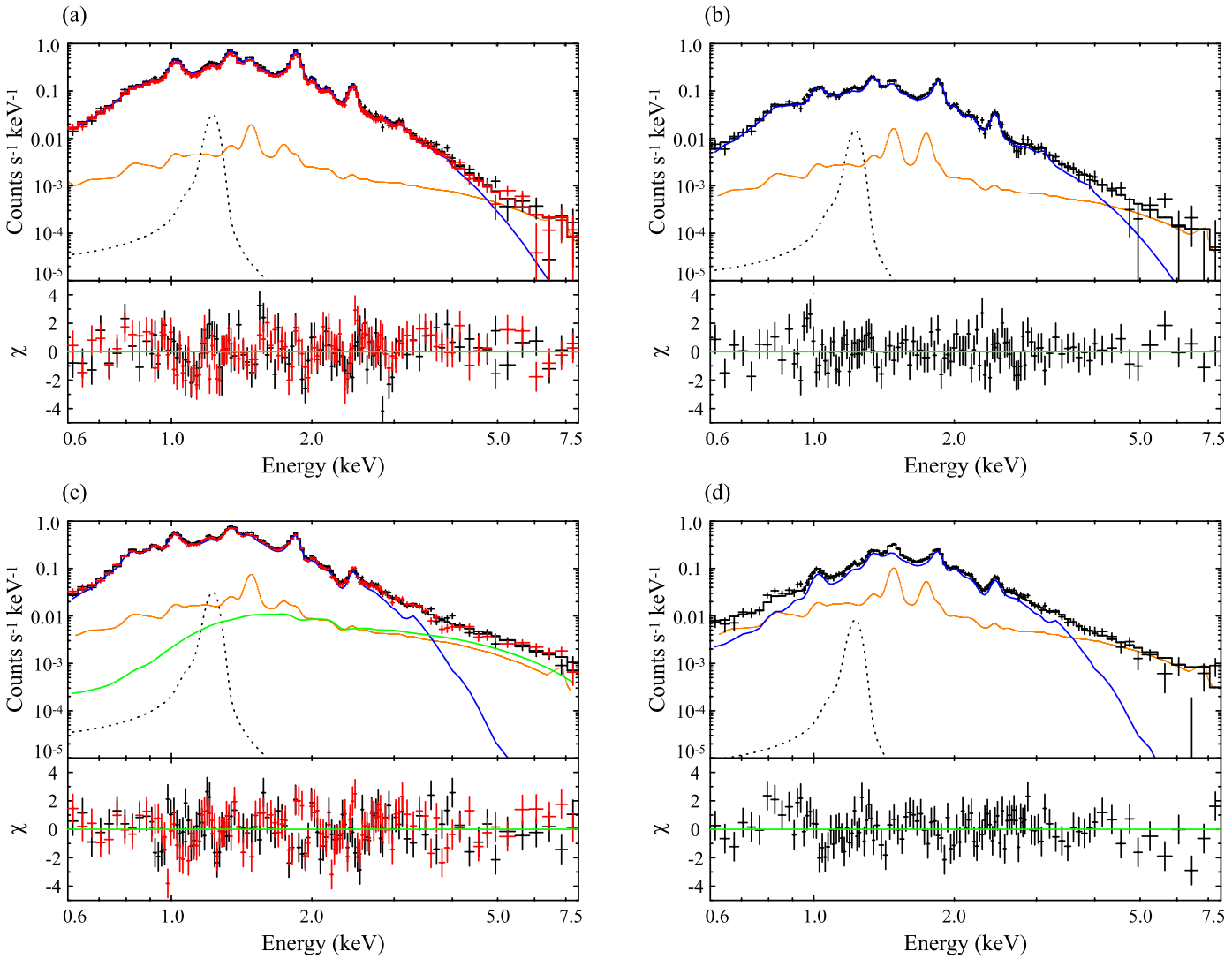

Figure 3. (a) MOS1 (red) and MOS2 (black) spectra from Region 1 plotted with the model without a Gaussian for Fe L lines (see the text for details). The blue, orange, and black curves represent the RP model, the background, and the sum of the models, respectively. The black dotted curve represent a Gaussian at 1.23 keV added to the model (the black dotted curve). (b)–(d) Same as (a) but for Regions 2–4. Since Region 3 is contaminated by the southern hard source (PSR B1853+01 and its pulsar wind nebula), the model includes a power law shown as the green curve. Only MOS2 data are available in Regions 2 and 4 because of a malfunction of the CCD chips of MOS1.

4.2. Physical Origin of RPs

We now discuss the physical origin of the RPs in W44 based on spatial distributions of the parameters such as kT_e and n_et, and their comparison with interacting gas distributions. Figure 6(a) shows a kT_e map. In panel (a-ii), we overlaid a ^{12}CO($J=2$–1)-to-^{12}CO($J=1$–0) intensity ratio map. The line ratio serves as a good indicator of shock–cloud interactions. A ratio well above the typical value in the unshocked part of the cloud, 0.6, indicates that the gas is shocked and/or heated (Yoshiike et al. 2013). The electron temperature kT_e tends to be lower at the locations where the ^{12}CO($J=2$–1)-to-^{12}CO($J=1$–0) ratio is higher. Similar tendencies were found also in other MM SNRs with RPs, IC 443 and W28 (Matsumura et al. 2017a; Okon et al. 2018). Those authors claimed that the tendencies are most probably explained by thermal energy exchanges between the plasmas and clouds via thermal conduction (Zhang et al. 2019). Thus, our result on W44 would also be suggestive of significant thermal conduction between the X-ray-emitting plasma and interacting gas.

Information from another parameter, n_et, whose spatial distribution is presented in Figure 6(b), has revealed far more convincing evidence for thermal conduction. In Figure 7, we plot kT_e and n_et derived for each subregion. The data points are divided into two groups. The blue points come from regions where Seta et al. (2004) discovered ^{12}CO($J=1$–0) lines broader than $\Delta V = 7$ km s^{-1} in full width at half maximum (see panels (a-iii) and (b-iii) of Figure 6 and also Figure 7(a) for the locations), referred to as spatially extended moderately broad emission (SEMBE) by Seta et al. (2004). The red points, on the other hand, are from the other regions. The two groups are clearly separated from each other, and each of the two groups shows a clear anticorrelation between kT_e and n_et.

The result in Figure 7(b) can be well understood in the context of the thermal conduction scenario as follows. Let us assume that the X-ray-emitting plasma initially had an ionization degree close to CIE ($n_et \sim 10^{12}$ cm^{-3} s) and an electron temperature of $kT_{\rm init} \sim 1$ keV as we assumed in the

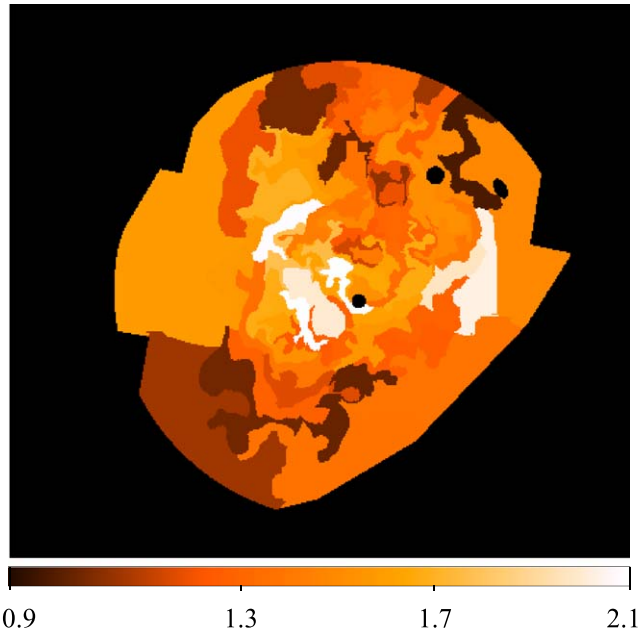

Figure 4. Reduced chi-squared map.

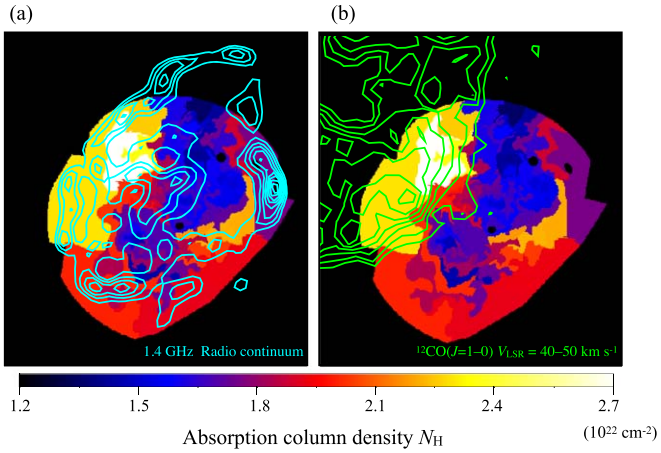

Figure 5. Distribution of X-ray absorption column density ($N_{\rm H}$). The same radio continuum image as that in Figure 1(a) is overlaid as cyan contours in panel (a). The green contours in (b) denote ^{12}CO($J = 1$–0) emissions in a velocity range of $V_{\rm LSR} = 40$–50 km s^{-1} as observed with the Nobeyama 45 m radio telescope in the FUGIN project (Umemoto et al. 2017).

spectral fittings in Section 3.3. After the shock encountered the molecular cloud, the plasma was rapidly cooled due to thermal conduction. At this point, the plasma switched into an overionized state since the cooling proceeded on a timescale shorter than the recombination rate. Once the cooling rate became slower, recombination started to dominate to make the ionization degree gradually approach CIE. What we are currently observing in W44 would be emission from the plasma in this phase. Figure 7(c) presents schematic trajectories of the plasma on the kT_e–n_et plane in the above scenario. The clear separation between the SEMBE and non-SEMBE regions suggests that the plasma was more efficiently cooled in the SEMBE regions.

Although the nature of the SEMBE is not yet clear, a plausible interpretation would be that the SEMBE is emitted by unresolved dense clumps shocked and disturbed by the SNR shock (Seta et al. 2004; Sashida et al. 2013). Since those clumps are embedded in the hot X-ray-emitting plasma, cloud evaporation would occur through thermal conduction between the plasma and the clumps, making the plasma in the SEMBE regions efficiently cooled. Cloud evaporation in SNRs have been numerically studied using hydrodynamical simulations (e.g., Zhou et al. 2011; Zhang et al. 2019) as well as with magnetohydrodynamical simulations (e.g., Orlando et al. 2008). According to the result by Zhang et al. (2019), cloud evaporation plays a role in rapid cooling of hot plasma and thus also in overionization. Sashida et al. (2013) estimated the clumps in the SEMBE region have a size of $\ll$0.3 pc. The typical evaporation timescale of the clumps through thermal conduction can be evaluated as $t_{\rm evap} \approx 5.4 \times 10^{10}\ (n_e/1\ {\rm cm}^{-3})(l/1\ {\rm pc})^2(kT_e/1\ {\rm keV})^{-5/2}$ s $\ll 10^{11}$ s (e.g., Orlando et al. 2005), assuming the plasma density $n_e = 1\ {\rm cm}^{-3}$, the clump size $l \ll 0.3$ pc, and the average plasma temperature $kT_e = 0.3$ keV. The evaporation timescale is sufficiently smaller than the timescale for a plasma to reach CIE ($t_{\rm CIE} \approx 10^{12}(n_e/1\ {\rm cm}^{-3})^{-1}$ s) and, therefore, cloud evaporation can make the plasma overionized. ALMA would be able to resolve dense clumps of the SEMBE gas in W44 as pointed out by Sashida et al. (2013). Spatially resolved spectroscopy in X-rays with angular scales similar to that of ALMA then should observationally reveal the process of cloud evaporation and resulting overionization.

In addition to the present result, which has provided clear evidence for thermal conduction as the origin of the overionization in W44, recent studies suggest that the same mechanism seems responsible for RPs in other SNRs as well: G166.0+4.3 (Matsumura et al. 2017b), W28 (Okon et al. 2018), and CTB 1 (Katsuragawa et al. 2018). A clear exception is W49B. Analyzing *NuSTAR* data of W49B, Yamaguchi et al. (2018) found a result opposite to this, a positive correlation between kT_e and n_et. The correlation can be well explained by an efficient cooling by adiabatic expansion in low-density areas. The result led Yamaguchi et al. (2018) to conclude that adiabatic expansion plays a predominant role in overionizing the plasma in W49B. Then, what determines the main channel for rapid cooling? An important hint would be the young age of W49B (1–6 kyr: Pye et al. 1984; Smith et al. 1985) in the category of MM SNRs containing RPs. Cooling through adiabatic expansion is expected to work efficiently in the early phase of SNR evolution when the blast wave breaks out of dense circumstellar matter into tenuous ISM (Itoh & Masai 1989; Shimizu et al. 2012). In contrast, thermal conduction can be effective only after the blast wave hits dense ambient ISM, and thus would be expected to be predominant at later stages. Based on hydrodynamical simulations, Zhang et al. (2019) reached a similar conclusion: that both thermal conduction and adiabatic expansion contribute to plasma cooling in SNRs and that the dominant channel can be changed as SNRs evolve. Systematic observational studies as well as their comparison with theoretical and numerical studies are necessary to further clarify the overionization process in SNRs.

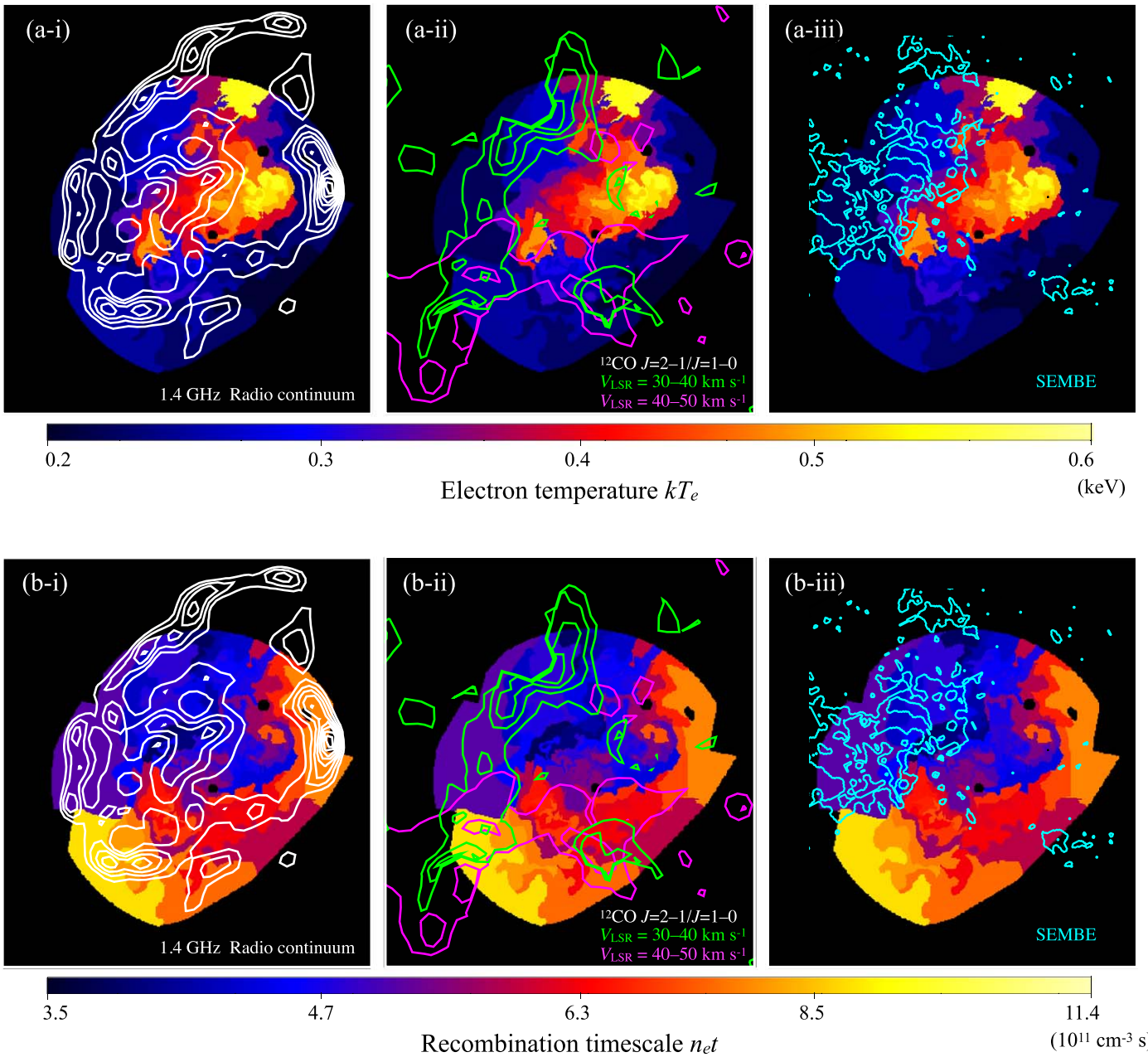

Figure 6. Maps presenting the distributions of (a) kT_e and (b) n_et. The white contours in (a-i) and (b-i) indicate the same radio continuum image as that in Figure 1(a). The green and magenta contours in (a-ii) and (b-ii) denote a ^{12}CO(J = 2–1)-to-^{12}CO(J = 1–0) intensity ratio map drawn every 0.1 from 0.7 in V_{LSR} = 30–40 km s^{-1} and V_{LSR} = 40–50 km s^{-1} taken from Yoshiike et al. (2013). The velocity ranges correspond to that of the giant molecular cloud interacting with W44. In (a-iii) and (b-iii), the cyan contours denote the half-intensity line width diagram for the ^{12}CO(J = 1–0) in V_{LSR} = 20–60 km s^{-1} obtained with the Nobeyama 45 m radio telescope by Seta et al. (2004). Each contour represents 7, 10, and 13 km s^{-1}.

5. Conclusion

We have performed spatially resolved spectroscopy of X-ray emission of W44 obtained with *XMM-Newton* deep observations, in order to clarify the physical origin of overionization of the X-ray-emitting plasma. All spectra extracted from each region are well fitted with an RP model. The X-ray absorption column densities correlate well with the distribution of foreground gas in the line of sight toward W44 as traced by radio line emissions reported in the literature. The obtained electron temperature kT_e and the recombining timescale n_et of RPs range from 0.18 keV to 0.60 keV and from 3×10^{11} cm^{-3} s to 9×10^{11} cm^{-3} s, respectively. We have discovered that kT_e is lower in the region where W44 is interacting with molecular clouds and that kT_e and n_et are negatively correlated. These findings indicate thermal conduction between X-ray-emitting plasma and the cold dense gas as the origin of the overionization. We have also found that n_et is especially small in the regions with spatially extended, moderately broad emissions of ^{12}CO(J = 1–0) lines, which are considered to be emitted by clumpy gas shocked and disturbed by the SNR shock (Seta et al. 2004; Sashida et al. 2013). This result can be explained by a rapid cooling of the plasma through evaporation of the clumpy gas. A comparison between our result on W44 and that on W49B (Yamaguchi et al. 2018) prompts us to consider that both thermal conduction and adiabatic cooling are possible channels of

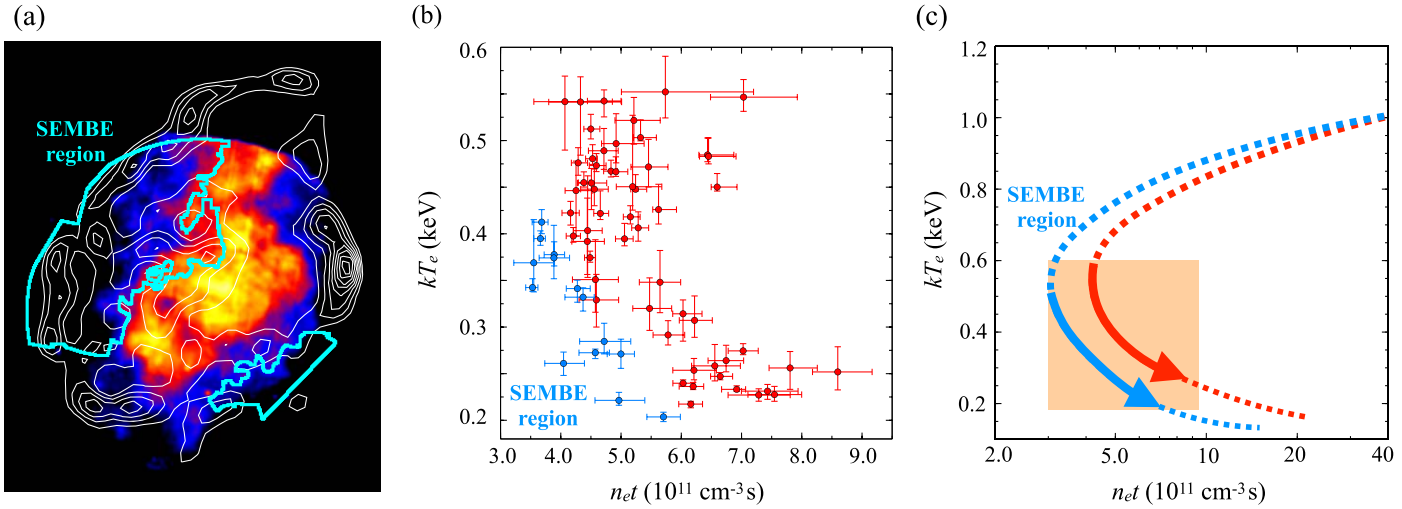

Figure 7. (a) Same as Figure 1(a) but with the definition of the SEMBE regions in cyan. (b) Relationship between n_et and kT_e. The blue points are from the SEMBE regions whereas the red points are from the other regions. (c) Schematic trajectories of plasma during its evolution after a shock–cloud collision. The color scheme is the same as that of panel (b). The shaded area corresponds to the range plotted in (b).

overionization in SNRs and that the dominant channel may change as SNRs evolve. Recent hydrodynamical simulations by Zhang et al. (2019) support this idea as well.

We deeply appreciate all the *XMM-Newton* and NANTEN2 team members. This work is partially supported by JSPS/MEXT Scientific Research grant Nos. JP19J14025 (H.O.), JP19H01936 (T.T.), JP25109004 (T.T. and T.G.T.), JJP19K03915 (H.U.), JP15H02090 (T.G.T.), and ASI-INAF no. 2017-14-H.O (S.O., M.M., and F.B.).

ORCID iDs

Takaaki Tanaka https://orcid.org/0000-0002-4383-0368
Hiroya Yamaguchi https://orcid.org/0000-0002-5092-6085
Takeshi Go Tsuru https://orcid.org/0000-0002-5504-4903
Randall K. Smith https://orcid.org/0000-0003-4284-4167
Satoshi Yoshiike https://orcid.org/0000-0002-2458-7876
Salvatore Orlando https://orcid.org/0000-0003-2836-540X
Marco Miceli https://orcid.org/0000-0003-0876-8391

References

Arnaud, K. A. 1996, in ASP Conf. Ser. 101, Astronomical Data Analysis Software and Systems V, ed. G. H. Jacoby & J. Barnes (San Francisco, CA: ASP), 17
Claussen, M. J., Frail, D. A., Goss, W. M., & Gaume, R. A. 1997, ApJ, 489, 143
Claussen, M. J., Goss, W. M., Frail, D. A., & Desai, K. 1999, ApJ, 522, 349
Foster, A. R., Smith, R. K., & Brickhouse, N. S. 2017, in AIP Conf. Proc 1811, Atomic Processes in Plasmas, ed. D. Benredjem (Melville, NY: AIP), 1811, 190005
Frail, D. A., & Mitchell, G. F. 1998, ApJ, 508, 690
Greco, E., Miceli, M., Orlando, S., et al. 2018, A&A, 615, A157
Harrus, I. M., Hughes, J. P., Singh, K. P., Koyama, K., & Asaoka, I. 1997, ApJ, 488, 781
Itoh, H., & Masai, K. 1989, MNRAS, 236, 885
Jones, L. R., Smith, A., & Angelini, L. 1993, MNRAS, 265, 631
Katsuragawa, M., Nakashima, S., Matsumura, H., et al. 2018, PASJ, 70, 110
Kawasaki, M., Ozaki, M., Nagase, F., Inoue, H., & Petre, R. 2005, ApJ, 631, 935
Kawasaki, M. T., Ozaki, M., Nagase, F., et al. 2002, ApJ, 572, 897
Kuntz, K. D., & Snowden, S. L. 2008, A&A, 478, 575
Kushino, A., Ishisaki, Y., Morita, U., et al. 2002, PASJ, 54, 327
Leahy, D. A., & Tian, W. W. 2007, A&A, 461, 1013
Lopez, L. A., Pearson, S., Ramirez-Ruiz, E., et al. 2013, ApJ, 777, 145
Lumb, D. H., Warwick, R. S., Page, M., & De Luca, A. 2002, A&A, 389, 93
Matsumura, H. 2018, PhD thesis, Kyoto Univ.
Matsumura, H., Tanaka, T., Uchida, H., Okon, H., & Tsuru, T. G. 2017a, ApJ, 851, 73
Matsumura, H., Uchida, H., Tanaka, T., et al. 2017b, PASJ, 69, 30
Miceli, M., Bocchino, F., Decourchelle, A., et al. 2010, A&A, 514, L2
Nobukawa, K. K., Nobukawa, M., Koyama, K., et al. 2018, ApJ, 854, 87
Okon, H., Uchida, H., Tanaka, T., Matsumura, H., & Tsuru, T. G. 2018, PASJ, 70, 35
Orlando, S., Bocchino, F., Reale, F., Peres, G., & Pagano, P. 2008, ApJ, 678, 274
Orlando, S., Peres, G., Reale, F., et al. 2005, A&A, 444, 505
Ozawa, M., Koyama, K., Yamaguchi, H., Masai, K., & Tamagawa, T. 2009, ApJL, 706, L71
Petre, R., Kuntz, K. D., & Shelton, R. L. 2002, ApJ, 579, 404
Pye, J. P., Becker, R. H., Seward, F. D., & Thomas, N. 1984, MNRAS, 207, 649
Ranasinghe, S., & Leahy, D. A. 2018, AJ, 155, 204
Rho, J., & Petre, R. 1998, ApJL, 503, L167
Sanders, J. S. 2006, MNRAS, 371, 829
Sashida, T., Oka, T., Tanaka, K., et al. 2013, ApJ, 774, 10
Seta, M., Hasegawa, T., Dame, T. M., et al. 1998, ApJ, 505, 286
Seta, M., Hasegawa, T., Sakamoto, S., et al. 2004, AJ, 127, 1098
Sezer, A., Ergin, T., Yamazaki, R., et al. 2019, MNRAS, 489, 4300
Shelton, R. L., Kuntz, K. D., & Petre, R. 2004, ApJ, 611, 906
Shimizu, T., Masai, K., & Koyama, K. 2012, PASJ, 64, 24
Smith, A., Jones, L. R., Peacock, A., & Pye, J. P. 1985, ApJ, 296, 469
Smith, A., Jones, L. R., Watson, M. G., et al. 1985, MNRAS, 217, 99
Strüder, L., Briel, U., Dennerl, K., et al. 2001, A&A, 365, L18
Turner, M. J. L., Abbey, A., Arnaud, M., et al. 2001, A&A, 365, L27
Uchida, H., Koyama, K., Yamaguchi, H., et al. 2012, PASJ, 64, 141
Uchida, H., Koyama, K., & Yamaguchi, H. 2015, ApJ, 808, 77
Uchiyama, H., Nobukawa, M., Tsuru, T. G., & Koyama, K. 2013, PASJ, 65, 19
Umemoto, T., Minamidani, T., Kuno, N., et al. 2017, PASJ, 69, 78
Wilms, J., Allen, A., & McCray, R. 2000, ApJ, 542, 914
Wolszczan, A., Cordes, J. M., & Dewey, R. J. 1991, ApJL, 372, L99
Yamaguchi, H., Ozawa, M., Koyama, K., et al. 2009, ApJL, 705, L6
Yamaguchi, H., Tanaka, T., Wik, D. R., et al. 2018, ApJL, 868, L35
Yoshiike, S., Fukuda, T., Sano, H., et al. 2013, ApJ, 768, 179
Zhang, G.-Y., Slavin, J. D., Foster, A., et al. 2019, ApJ, 875, 2
Zhou, X., Miceli, M., Bocchino, F., Orlando, S., & Chen, Y. 2011, MNRAS, 415, 244